Intensity and Morphology-Based Energy Minimization for the Automatic Segmentation of the Myocardium

A. Pednekar[1], I.A. Kakadiaris[1], U. Kurkure[1], R. Muthupillai[2], S. Flamm[3]
[1] Visual Computing Lab, Dept. of Computer Science, Univ. of Houston, Houston, TX
[2] Philips Medical Systems North America, Bothell, WA
[3] Dept. of Radiology, St. Luke's Episcopal Hospital, Houston, TX
e-mail: ioannisk@uh.edu

Abstract

The extraction of significant cardiac functional parameters such as ejection fraction and wall thickening depends on reliable detection of myocardial contours. However, the manual contour tracing process is cumbersome, time-consuming, and operator-dependent. These limitations have motivated the development of automated segmentation techniques for accurate and reproducible left ventricular (LV) segmentation. In this paper, we present our automatic LV myocardial surface extraction method, which combines a fuzzy affinity-based region segmentation approach with energy minimizing dynamic programming, and the elastically adaptive physics-based deformable model framework. We have applied this technique on MR data from eight asymptomatic volunteers with very encouraging qualitative and quantitative results.

1 Introduction

Cardiovascular disease (CVD) is the primary cause of death in the United States for the past eight decades [1]. In the most common form, CVD causes reduced blood flow to the myocardium causing anomalous cardiac function. Thus, clinical diagnosis, treatment, and follow-up of CVD requires accurate spatio-temporal visualization of the entire heart. Recent advances in Cardiac Magnetic Resonance Imaging (CMRI) make it possible to take the 3D images of the heart in desirable orientations over the entire cardiac cycle describing the internal structure and motion of the heart. Thus, CMR is ideal for the baseline assessment, as well as for follow up of clinical progression and for monitoring the effect of treatment in patients with heart failure [3]. CMR's 3D approach for non-symmetric ventricles and it's superior image quality make it preferred technique for volume and ejection fraction (EF) estimation in heart failure patients [2]. The high resolution multi-phase 3D cardiac examinations produce a large amount of data (typically 200 to 300 images per patient) to be analyzed for a comprehensive patient study. In order to diagnose a cardiac function abnormality, physicians are interested in delineating the endocardium and the epicardium. This enables them to measure the percent of blood being pumped out by the LV per heart beat (EF) and the wall thickening properties over the cardiac cycle, which are good clinical indicators of the global and local cardiac function. However, interpreting and analyzing the large amount of data to derive clinically useful information is quite a formidable task for any cardiologist. Automatic extraction of useful physiological information from 4D cardiac image data, to analyze cardiac morphology and function, requires high level image segmentation techniques. Most of the research towards automated segmentation of CMRI data mainly consists of three major approaches: 1) positioning of the boundary near the strongest local image features using the principle of energy minimization [15, 9, 19, 6] (these methods rely on user interaction for initialization of the shape and location of the object's boundaries), 2) three-dimensional analysis for functional analysis of cardiac images [5, 20, 10, 16, 13], and 3) incorporation of a priori knowledge regarding shape and dynamics of the heart for image segmentation like AAM [12] and AAMM [21] (these methods could be biased towards a "too normal" pattern of the LV and its dynamics). Research is ongoing on developing hybrid segmentation methods for the extraction of LV endocardial boundary surfaces by combining edge, region and shape information [14, 8, 7, 17].

Recent developments in cine imaging using steady state free precision sequences - balanced fast field echo (bFFE) - provide high intrinsic myocardial to blood pool contrast. However, these CMR images are inherently fuzzy in nature due to heart dynamics and partial voluming effect. The endocardium is composed of trabeculae carneae, which are projections of myocardial muscle into the LV cavity forming the endocardial boundary. The partial voluming effect causes the intensity level near the endocardium to be in between that of myocardium and the blood pool. This effect is pronounced near the apex of the heart, where trabeculae carneae are numerous and densely packed. Also the papillary muscles, which are conical projections of the myocardial muscle, have the same intensity response as the myocardium (in CMR). Thus, to delineate the papillary muscles attached to the LV endocardium and to obtain an accurate endocardial boundary one needs to use a priori information. Hence, the high contrast between the myocardium and the blood pool alone is not sufficient for automatic segmentation of the my-

ocardium. Similarly, poor intensity contrast between the myocardium and air-filled lungs makes the automatic epicardial boundary detection a significant challenge. In addition, there is a drop in the blood intensity from the base to the apex of the heart due to coil intensity falloff.

As mentioned above, the automation of the LV segmentation includes challenges related to the automatic localization of the LV in CMR scans, the inherently fuzzy nature of the MR scan due to heart dynamics, and the presence of the papillary muscles inside the LV cavity. We have developed a new segmentation technique for the myocardial segmentation of the bFFE short axis cardiac CMR data, which overcomes these challenges successfully. Our method uses a region dynamics map along with Hough transform to automatically localize the LV. Then, the intensity-based fuzzy affinity map is combined with the energy minimizing dynamic-programming approach to automatically extract the myocardial contours. Finally, an elastically adaptive physics-based deformable model provides the 3D myocardial surface.

Conceptually our approach towards automatic myocardial segmentation is very closely related to hybrid segmentation approach followed in [14, 8, 7]. Our main contributions are the following: 1) automatic estimation of the seed region of the LV using a region dynamics map; 2) automatic robust LV seed propagation using intensity-based fuzzy affinities and adaptive fuzzy connectedness; 3) extension of cost function to include energy terms from intensity-based fuzzy affinity and radial continuity; and 4) development of a new class of forces derived from intensity gradients, fuzzy-affinities and dynamic programming-based contour data for elastically adaptive physics-based deformable model. Thus, our method doesn't require user interaction at both the LV identification and the myocardial segmentation phases.

Our method for the automatic LV myocardial boundary detection has the following features: 1) it provides spatially and temporally continuous contours; 2) it is patient-specific; 3) it is non-invasive; 4) it doesn't require any external contrast enhancement agents. We have compared the results of our method against the results obtained with manual delineation performed by experienced radiologists (St. Luke's Episcopal Hospital) with very encouraging results. These initial results demonstrate the feasibility of using our automatic LV myocardial segmentation to compute the EF in clinical practice.

2 Method

In this section, we present our automatic LV myocardial surface extraction method, which combines the "fuzzy affinity"-based segmentation approach with energy minimizing dynamic programming and the elastically adaptive physics-based deformable model framework. Specifically, we acquire bFFE cine images of the heart. Then, a region dynamics map, which is a difference of the near end-diastolic phases' basal slices, is used to automatically localize the heart in the data. The detection of circular regions using the Hough transform in the region dynamics map is used to estimate the location of the LV in the basal slice. The initial estimation of the LV region provides intensity statistics for the LV blood and myocardium. This LV localization at basal slice is then propagated along the entire end-diastolic volume and along time with the help of the fuzzy affinity-based LV blood classification and adaptive fuzzy connectedness. The automatically localized LV centroids serve as origins to transform each slice of CMR data into polar coordinates. The myocardium is then segmented in the basal slice, in polar coordinates, using intensity-based fuzzy affinities. Radial shape constraints are imposed using a dynamic programming approach to detect the myocardial contours. Next, the estimated mean endo- and epicardial radii and myocardium intensity statistics are used to propagate the myocardial segmentation along the entire end-diastolic volume. Similarly, we propagate the myocardial contours along the time axis to segment the entire cine data. Finally, these myocardial boundaries are used to initialize an elastically adaptive deformable model of the LV. The remainder of this section describes our technique in more detail.

2.1 Data Acquisition

Studies were performed on the eight subjects (6m/2f) with normal sinus rhythm, with consent. Volunteers were imaged on a 1.5T commercial scanner (Philips Gyroscan NT-Intera) using Vector-cardiographic gating. The bFFE short-axis sequence was acquired to cover the entire LV. The acquisition parameters for a cine bFFE sequence were, TE/TR/flip: 3.2/1.6/55 deg; 38-40 msec temporal resolution. Figs. 1(a,b) depict the data from the eighth bFFE slice of phase-1 and phase-3 (Subject-6).

2.2 LV Localization using a Region Dynamics Map

The cine bFFE sequence allows motion detection within thoracic cavity, and the heart being most dynamic organ can be detected based on its motion. Furthermore, circularity of the LV can be utilized to detect the LV in CMR scan. To that end, we take the pixel by pixel intensity difference between the same basal slice of the LV at two different near end-diastolic phases to construct a region dynamics map of the thoracic cavity and then perform edge detection (Fig. 1(c)).

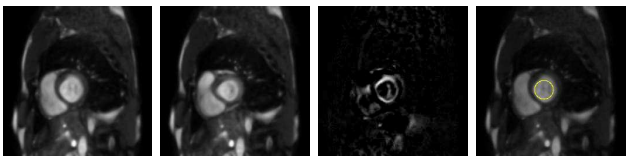

(a) (b) (c) (d)

Figure 1: (a,b) Slice 8 from phase-1 and 3 (Subject-6). (c) Region dynamics map a-b. (d) Detected circle for the estimation of the LV region.

The absence of papillary muscles attached to the endocardium in the basal slice results in a circular LV boundary. Other circular structures in the thoracic cavity are suppressed in a difference image due to their static nature. Thus, we observe a prominent circular region belonging to the LV in the thoracic cavity. Application of Hough transform easily detects the circle belonging to the LV boundaries (Fig. 1(d)). The center of this LV circle provides us the initial seed point for the LV and also for automatic cropping of CMR data to retain the area related to LV alone. The three primary tissues present in the cropped scans are the bright blood, gray myocardium, and dark air-filled lungs. Therefore, we use a greedy EM algorithm for Gaussian mixture learning [23] to fit a mixture of five Gaussians to the histogram (three for each tissue type, one for the partial voluming between blood and myocardium, and one for the partial voluming between myocardium and air). Thus, the local region just around the LV circle provides the initial sample statistics for the LV blood and the myocardium (Fig. 2).

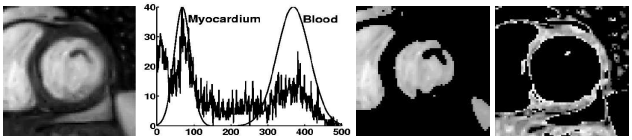

(a) (b) (c) (d)

Figure 2: (a) Slice 8 (Subject-5). (b) Gaussians for the myocardium and the blood. (c,d) Classified blood and myocardium.

This seed point and intensity statistics are then used for the initialization of entire LV cavity at the end-diastolic phase and also along all the phases.

2.3 Automatic Detection of Center Axis of the LV

Once the LV is localized in the data, we use the statistical information regarding intensity of the LV blood to classify parts of the data having similar intensity statistics. The fuzzy nature of the CMR data is accommodated for, by using fuzzy membership functions for the intensity-based classification purposes [22]. The membership function is based on the degree of intensity space adjacency globally and it classifies objects with similar intensities in the image data. The definition for a fuzzy affinity assumes intensity homogeneity function to be Gaussian in nature:

$$\mu_\kappa(c,d) = e^{-\frac{1}{2}[\frac{\frac{1}{2}(f(c)+f(d))-m_1}{s_1}]^2},$$

where m_1 and s_1 are the mean and standard deviation of the intensity of the target region.

The CMR data is a stack of planes parallel to each other. Although scattered over different slices, this data is connected to each other in terms of 3D spatial connectivity and normalized intensity similarity. We combine the intensity-based global pixel affinities with a priori knowledge regarding the slice by slice (or phase by phase) intensity, shape and size variations of the LV to detect the center axis of the LV. The basal LV localization is propagated along the entire volume by minimizing a cost function. The cost function is comprised of slice (or phase) specific intensity statistics, distance of the LV centroid to the previous slice (or phase) seed point, and the size variation compared to the size in the previous slice (or phase). The center axis' curvature information can be used as a tie breaker, if required. The cost function can be defined as follows:

$$\mu_S(p,n) = \beta_1\mu_I(p,n) + \beta_2\mu_D(p,n) + \beta_3\mu_Z(p,n),$$

where $\mu_S(p,n)$ indicates overall cost of given region being a target region, $\mu_I(p,n)$, $\mu_D(p,n)$, $\mu_Z(p,n)$, represent the cost due to intensity, distance from previous centroid and size of the region, p indicates predicted value for the target region in the current slice based on previous slices' (or phase's) statistics, and n is the corresponding current value for detected regions in current slice.

Due to coil intensity falloff, the average intensity of the LV blood pool drops off as we move towards the apex of the heart, making simple spatial 3D connectedness ineffective. In order to accommodate for the decreasing intensity, decreasing LV size and the higher degree of curvature of the LV near the apex, we pre-compute seeds for LV for every slice using the above cost function and then perform LV blood segmentation on each slice individually. The intensity falloff is tackled by updating the intensity statistics for every slice. The LV blood intensity statistics from the basal slice is used to classify the blood pool regions in the next slice using intensity-based global pixel affinities. The new seed in the next slice is then identified using the cost function. The LV blood pool intensity statistics are updated based on the new LV blood pool region, which also provides the size estimate of the LV. Then this seed, size, and intensity statistics are used in the next slice and similarly we get the new seed, size, and intensity statistics. Once we have intensity statistics, size, and seed for the previous and the current slice we can predict the seed, size, and the statistics for the next slice. In some cases, due to inconsistent breath hold, intensity prediction is not accurate enough. In those cases we correct it with estimated Gaussian for the blood in the next slice. However, EM-based blood intensity estimation is not accurate in basal slices as flow artifacts in LV result in two different Gaussians for the LV blood. The prediction is followed by the computation of the new cost function based on predicted and current values, thus propagating the seed through the end-diastolic LV volume. These LV regions are further refined using adaptive fuzzy connectedness-based image segmentation [18] to get better LV blood classification and hence better estimation of centroids.

This approach helps us overcome the challenges posed in automatically detecting LV blood pool in the entire volume. The advantage of this method is that even though the seed does not fall in the LV region due to high curvature, the computation of affinity over the entire image along with the cost function provides an estimate of where the LV is located in

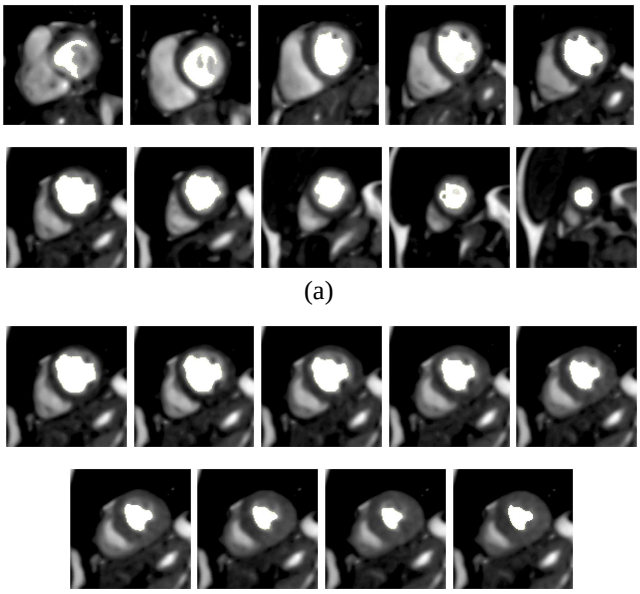

(a)

(b)

Figure 3: (a) End-diastolic slices (Subject-6) overlaid with automatically propagated LV blood pool regions. (b) LV blood propagation from the end-diastolic to the end-systolic phase (Subject-6).

the next slice. Fig. 3 depicts results of LV propagation using this method along the LV volume and along time.

2.4 Segmentation of the Myocardium

All the end-diastolic bFFE slices are then converted into polar coordinates using the previously identified LV centroids as the center of origin (Fig. 4 (a)). The intensity-based fuzzy affinities for myocardium are computed in polar coordinates using myocardium intensity statistics obtained from estimated Gaussian for myocardium (Fig. 4 (b)). The fuzzy membership helps classify pixels on the endocardial boundary affected by partial voluming.

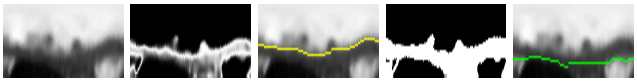

(a) (b) (c) (d) (e)

Figure 4: Contour extraction in polar coordinates. (a) Slice 8 (Subject-6) polar image, (b) myocardial affinity map, (c) extracted endocardial contour, (d) binarized myocardial affinity map, and (e) extracted epicardial contour.

A gradient operator detecting a dark region above a bright region is applied to these affinity images. Thus, we obtain very good endocardial boundaries overcoming the presence of papillary muscles to large extent (Fig. 4(c)). However, the estimates for epicardial boundaries are not satisfactory due to very low intensity contrast between the myocardium and the air in the lungs. We overcome this problem by first binarizing the myocardium affinity image (Fig. 4(d)) and then detecting bright over dark edges to extract the epicardial boundary (Fig. 4(e)). In addition, to obtain spatially continuous endo- and epicardial contours we add a spatial continuity constraint in polar coordinates.

2.5 Contour Smoothing Through Dynamic Programming

The segmentation of CMR data typically poses two challenges: the determination of the tissue boundary, and the delineation of the LV boundary. The partial voluming effect blurs the intensity distinction between the neighboring tissue types. Thus, separability of tissues based on intensity statistics alone is not accurate. In addition, the neighboring tissues though of the same type need not belong to the same anatomical structures (e.g., trabeculae carneae and papillary muscles projecting out of the myocardium). Thus, it is not possible to delineate the myocardium based on the tissue border detection alone. The above mentioned challenges underline the need for incorporating a priori information regarding the geometry of the LV to the intensity-based segmentation.

The gradients of the myocardium affinity image provide boundaries located almost in the horizontal direction in the polar coordinates. The optimal myocardial contour is the contour which follows the high myocardial affinity and high myocardial affinity gradient closely, while maintaining a high degree of spatial continuity in the tangent direction. The dynamic programming approach is used to detect the horizontal myocardial edges by finding the optimal path between the two borders of the polar affinity image. Any possible boundary can be represented as a polyline with N vertices $(P_1, P_2, P_3, ..., P_N) \in P$. For a polyline to be a valid boundary, it should have minimum cost for the cost function $C_{sum} = \sum_{j=1}^{N} C(P_j)$. The cost function for the polar myocardial affinity image is expressed as:
$C(P_j) = -\omega_{ia} C_{ia}(P_j) - \omega_{ga} C_{ga}(P_j) - \omega_r C_r(P_{j-1}, P_j)$, where $\omega_{ia}, \omega_{ga}, \omega_r$ are the weights for the myocardial affinity value C_{ia}, the myocardial affinity gradient C_{ga}, and the radial distance between pixels on the polyline in adjacent columns C_r. The affinity value term forces the boundary to follow the homogeneous path through the pixels with high myocardial affinity. The affinity gradient term is responsible for moving the boundary towards the points having strong myocardial affinity gradient in a direction perpendicular to the boundary. The continuity term restricts the boundary from taking big steps in radial direction between the adjacent pixels along the horizontal boundary. This term imposes the spatial continuity constraint, smoothing out the boundary in the horizonal direction. The continuity term can be implemented either as the linear or the second order continuity term. The second order term allows smoother transitions of the boundary in the vertical direction. The boundary detection by dynamic programming is computationally very efficient since there is no need to do the exhaustive search for

the optimal solution. The weights of different terms in the cost function are trained for particular application-specific features.

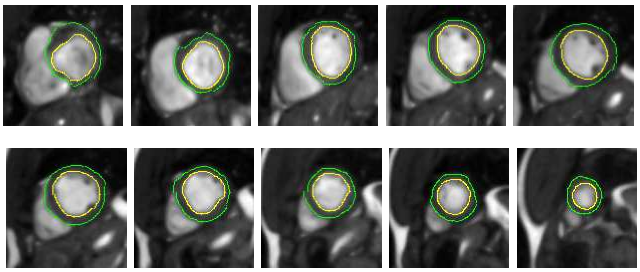

(a)

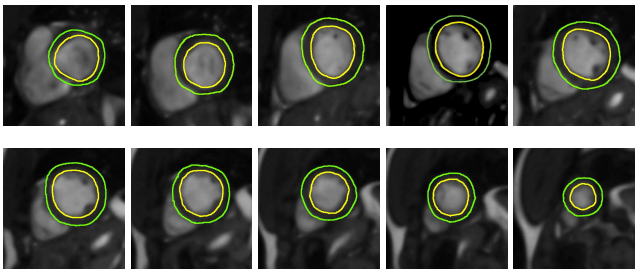

(b)

Figure 5: (a) Extracted myocardial contours using dynamic programming. (b) Projections of the fitted elastically adaptive deformable model for the end-diastolic phase (Subject-6).

This results in spatially continuous endo- and epicardial boundaries (Fig. 4 (c,e)). Fig. 5 (a) depicts the results obtained for the myocardial boundaries mapped back into Euclidean coordinate system.

2.6 Fitting of Elastically Adaptive Deformable Model

Once 2D contours are detected in each slice, we employ 3D energy functionals derived from intensity, fuzzy affinity, contour data, and 3D spatial continuity to obtain a minimal energy surface pertaining to the myocardium. To extract and reconstruct the myocardial surface from the 3D data, we employ an elastically adaptive physics-based deformable surface model [11, 17]. The domain-specific prior knowledge of the myocardial boundary is incorporated to optimize the fitting of the deformable model. The elasticity parameters of the deformable model are changed adaptively, depending on the energy function values, allowing us to overcome 3D discontinuities. The 3D deformable model of the LV and the myocardium is initialized using the LV centroids and mean endo- and epicardial radii information already available. The model overcomes 2D discontinuities like contours not closing properly and dents in the contour due to papillary muscles (Fig. 5 (b)). In addition, the model overrides the 3D discontinuities that might be present in endo- and epicardial boundaries mostly due to the papillary muscles, the low myocardium to lungs contrast, and the high curvature of LV near apex.

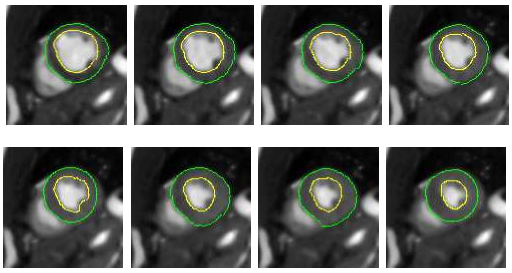

Figure 6: Extracted myocardial contours for the central slice from the end-diastolic to the end-systolic phase (Subject-6).

The myocardial contours extracted at the end-diastolic phase are then propagated along time (Fig. 6) till the end-systolic phase (Fig. 7).

3 Results and Evaluation

In this paper, we present the validation of the 2D myocardial contours before fitting the deformable model as the accuracy of this data governs the final myocardial segmentation. We compared these contours against the manually traced endo- and epicardial boundaries. Comparisons were carried out for only those slices in which automatically generated contours were present.

The manual tracing by two experienced radiologists from a St. Luke's Episcopal hospital for the endocardial and epicardial contours on each slice of the LV at the end-diastolic and end-systolic phase using Easy Vision (Philips Medical Systems, Release 5.0) served as the independent standard. A separate post-processing workstation was used to extract endocardial and epicardial contours and compute the EF using our algorithm.

There are two main parts in our validation process: 1) representation of errors in an anatomy-centered frame of reference, and 2) geometric error computations.

Anatomy-Centered Frame of Reference: We use a 17-segment LV model for reporting the distribution of different local geometric errors for the myocardial contour extraction in short-axis images [4].

In this model, the LV is divided into equal thirds perpendicular to the long axis of the heart generating basal, mid-cavity, and apical slices (Fig. 8). The basal third starts from the area extending from the mitral annulus to the tips of the papillary muscles at end-diastole. The mid-cavity region includes the entire length of the papillary muscles. The apical section is the area beyond the papillary muscles to apex of the LV cavity. The true apex or apical cap is the area (segment 17) of myocardium beyond the end of the LV cavity. Our algorithm does not segment the myocardium beyond the LV cavity, so we restrict our error reports only to the 16 segments. In addition, only slices containing myocardium in all 360^0 are selected (due to the complex mixing of myocardium

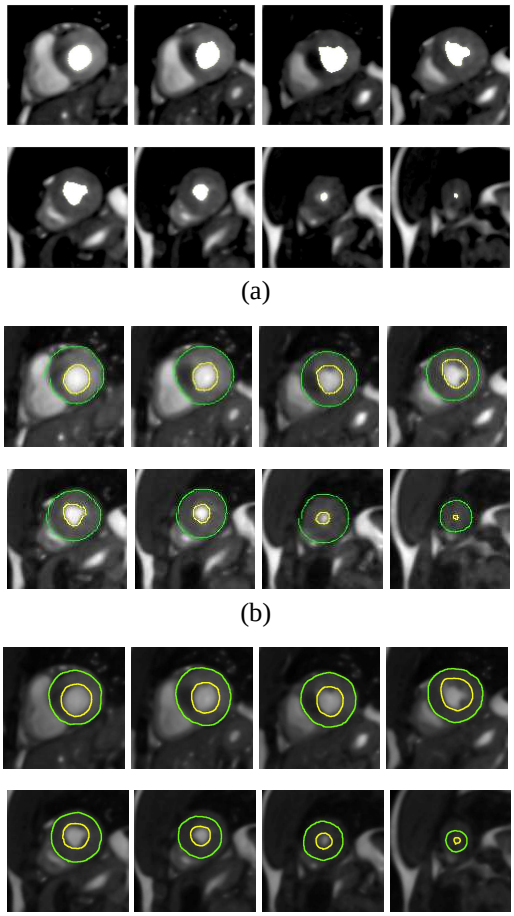

Figure 7: (a) End-systolic slices (Subject-6) overlaid with automatically propagated LV blood pool regions. (b) Extracted myocardial contours by dynamic programming. (c) Projection of the fitted elastically adaptive deformable model for the end-systolic phase (Subject-6).

and connective tissue at the base of the heart, especially the septum). The basal, mid-cavity, and apical segments define the location along the long axis of the ventricle from the apex to the base. Concerning the circumferential location, the basal and mid-cavity slices are divided into six segments. The anterior and posterior inter-ventricular grooves serve as the landmarks for determining the six segments. Similarly, the apical slices are partitioned into four sectors (the septal sector and three equal subsectors for the lateral sector). These segments are transformed into a bull's-eye map, which maps the basal slices as the outer ring and the apical slices as the innermost ring.

Geometric Error Indices: To quantitatively assess the accuracy of the automatically extracted contours with respect to manual contours we use following indices.

A. Border positioning errors: The automatically detected contours were quantitatively assessed for the positioning error in terms of radial distance of each point from the corresponding point on the manually traced contour (Fig. 9).

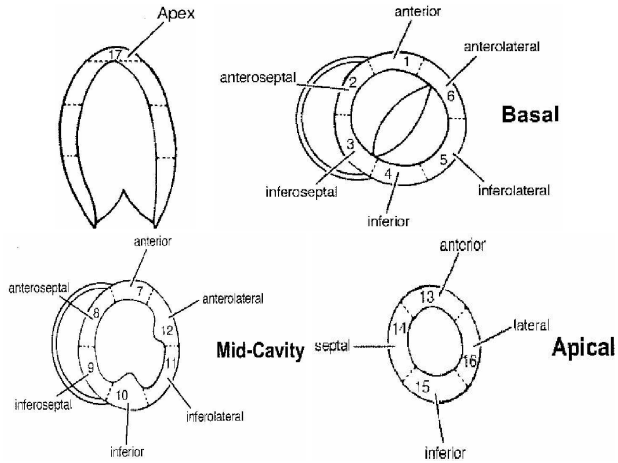

Figure 8: The 17 segment LV model [4].

The error magnitude effectively captures the effect of error on the LV volume, EF, and WT computations. Epicardial contour detection is more difficult at the lateral portion of the myocardium in the apical and the mid-ventricular slices.

B. Area Measurements: The error in area computation was assessed using regression analysis and Bland-Altman analysis for all the slices from all subjects. Fig. 10 depicts a very good correlation between the endocardial areas traced manually and the ones extracted by our method. The bias and the limits of agreement are comparable to the inter-observer variability inherent in manual methods.

C. Wall thickness: The wall thickness (WT) is computed as the radial distance between the endo- and epicardial contours. Figs. 11(a,b) depict the mean and standard deviation of error in WT computation with respect to the manual contours. The WT error is higher at the lateral side in the apical and the mid-ventricular slices.

D. Ejection Fraction: The agreement between the EF computation by the automatic and the manual method was assessed using Bland and Altman's method. The EF computations are carried out only for the slices in which automatically generated contours were present. The EF computed using these two methods are in good agreement. Specifically,

Reader 1: mean bias in EF (in %): +4.4 +/- 5.7; limits of agreement (+/- 2SD): -7.0 to +15.8 (Fig. 12(a)).

Reader 2: mean bias in EF (in %): 0.63 +/- 4.7; limits of agreement (+/- 2SD): -8.8 to 10.1 (Fig. 12(b)).

The inter-observer variability between the two readers is as follows: mean bias in EF (in %): -3.8 +/- 3.4; limits of agreement (+/- 2SD): 3.2 to -10.7 (Fig. 12(c)).

Our preliminary results indicate that our automatic algorithm estimates the EF reliably, and the bias and the limits of agreement are comparable to inter-observer variability inherent in manual methods.

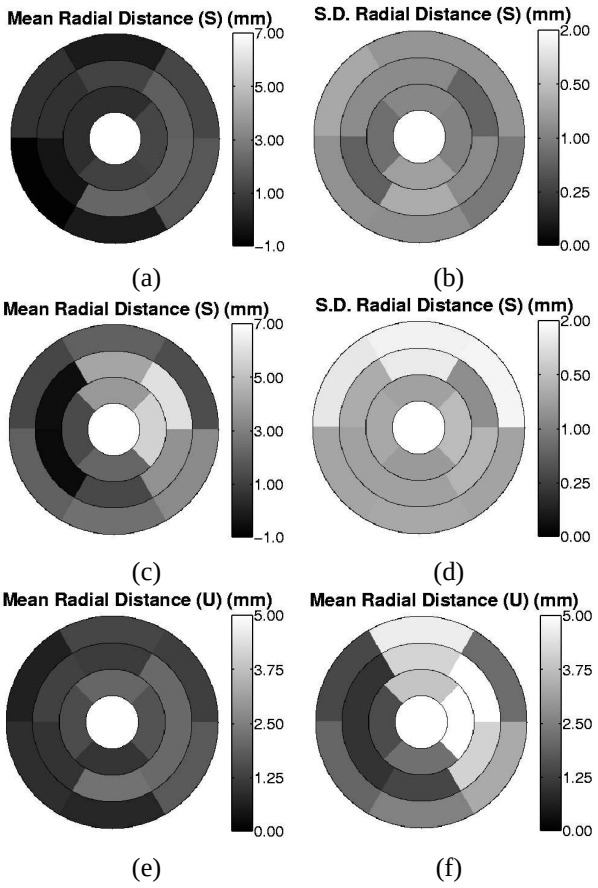

Figure 9: Mean and standard deviation of signed radial distance error for the (a,b) endocardial and the (c,d) epicardial contours. Unsigned error for the (e) endocardial and (f) epicardial contours.

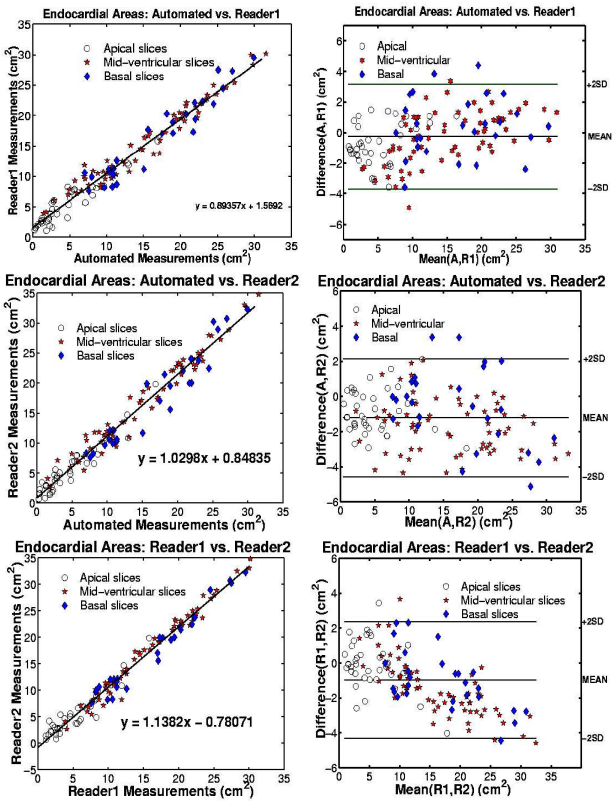

Figure 10: Linear regression and Bland-Altman plots for endocardial area measurements.

4 Discussion and Conclusion

The trabeculae carneae near the apex and the dorsal wall, and the two principal papillary muscles near the sternocostal wall and the diaphragmatic wall, projecting out of the myocardial wall, pose challenges to the automatic extraction of myocardial contours. The lateral epicardial boundary is blurred due to very low contrast between the myocardium and the air in the lungs. The effect of these factors on the automatic contour extraction are depicted in (Fig. 9). Observing these figures, the reader can easily infer that the endocardial boundary extraction successfully overcomes the challenges posed by the papillary muscles. However, the epicardial boundary detection suffers at the myocardium and lung boundary, thus introducing error in the WT estimates for those segments.

The qualitative and quantitative results obtained from our algorithm are very encouraging. The results indicate the reliability of the estimates of the EF. The bias and the limits of agreement are comparable to inter-observer variability inherent in manual methods. Further comprehensive clinical validation using data from thirty cases is currently underway.

References

[1] American Heart Association. Heart and stroke statistical update, 2001.

[2] N.G. Bellenger, M.I. Burgess, S.G. Ray, A. Lahiri, A.J. Coats, J.G. Cleland, and D.J. Pennell. Comparison of left ventricular ejection fraction and volumes in heart failure by echocardiography, radionuclide ventriculography and cardiovascular magnetic resonance; are they interchangeable? *European Heart Journal*, 21(16):1387–96, Aug 2000.

[3] N.G. Bellenger, J.M. Francis, C.L. Davies, A. Coats, and D.J.Pennell. Establishment and performance of a magnetic resonance cardiac function clinic. *Journal of Cardiovascular Magnetic Resonance*, 2(1):15–22, 2000.

[4] M.D. Cerqueira, N.J. Weissman, V. Dilsizian, A.K. Jacobs, S. Kaul, W.K. Laskey, D.J. Pennell, J.A. Rumberger, T. Ryan, and M.S. Verani. Standardized myocardial segmentation and nomenclature for tomographic imaging of the heart: A statement for healthcare professionals from the cardiac imaging committee of the council on clinical cardiology of the american heart association. *Circulation*, 105:539–542, January 2002.

[5] A.F. Frangi, W.J. Niessen, and M.A. Viergever. Three-dimensional modeling for functional analysis of cardiac images: A review. *IEEE Trans. Med. Imaging*, 20:2–25, 2001.

[6] D. Geiger, A. Gupta, L.A. Costa, and J. Vlontzos. Dynamic programming for detecting, tracking, and matching deformable contours. *IEEE Transactions on Pattern Analysis and Machine Intelligence,*, 17(3):294–302, 1995.

[7] C. Imielinska, D. Metaxas, J. Udupa, Y. Jin, and T. Chen. Hybrid segmentation of anatomical data. In *Proceedings of the 4th International Conference on Medical Image Computing & Computer-Assisted Intervention*, pages 1048–1057, Utrecht, The Netherlands, October 2001. Springer-Verlag.

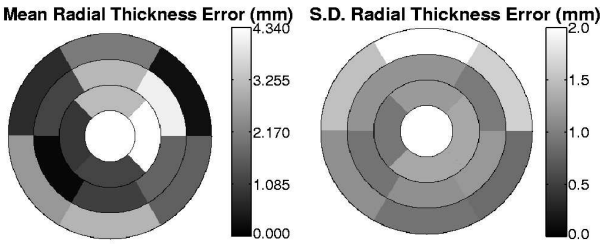

(a) (b)

Figure 11: Bull's-eye map for the WT error.

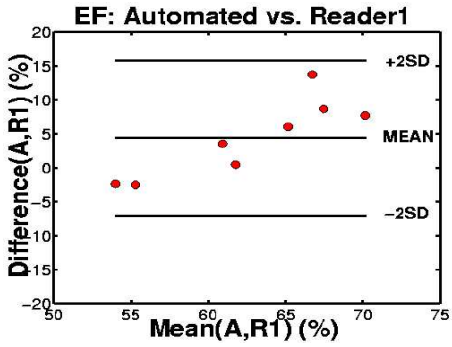

(a)

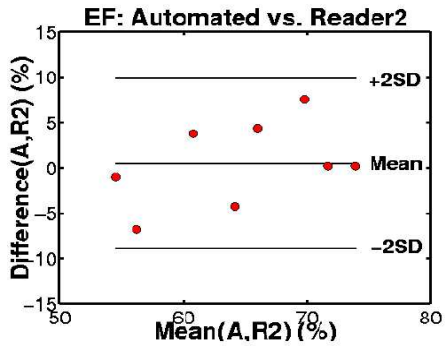

(b)

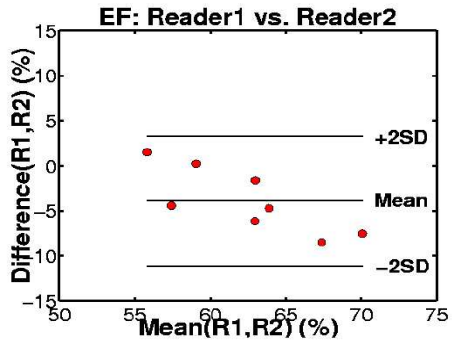

(c)

Figure 12: Bland-Altman plots for EF.

[8] M.P. Jolly. Combining edge, region, and shape information to segment the left ventricle in cardiac MR images. In *Proceedings of the 4th International Conference on Medical Image Computing & Computer-Assisted Intervention*, pages 482–490, Utrecht, The Netherlands, October 2001. Springer-Verlag.

[9] B.P.F. Lelieveldt, R.J. van der Geest, M. Ramze Rezaee, J.G. Bosch, and J.H.C. Reiber. Anatomical model matching with fuzzy implicit surfaces for segmentation of thoracic volume scans. *IEEE Trans. on Medical Imaging*, 18(3):218–230, Mar 1999.

[10] T. McInerney and D. Terzopoulos. A dynamic finite element surface model for segmentation and tracking in multidimensional medical images with application to cardiac 4D image analysis. *Computerized Medical Imaging and Graphics*, 19(1):69 – 83, January 1995.

[11] D. Metaxas and I.A. Kakadiaris. Elastically adaptive deformable models. *IEEE Transactions on Pattern Analysis and Machine Intelligence*, 24(10):1310–1321, 2002.

[12] S.C. Mitchell, J.G. Bosch, B.P.F. Lelieveldt, R.J. van der Geest, J.H.C. Reiber, and M. Sonka. 3-D active appearance models: segmentation of cardiac MR and ultrasound images. *IEEE Trans. on Medical Imaging*, 21(9):1167 –1178, 2002.

[13] A. Montillo, D. Metaxas, and L. Axel. Automated correction of background intensity variation and image scale standardization in 4D cardiac SPAMM-MRI. In *Medical Image Computing and Computer Assisted Intervention*, pages 620–633, Tokyo, Japan, September 25-28 2002.

[14] N. Paragios. A variational approach for the segmentation of the left ventricle in cardiac image analysis. *International Journal of Computer Vision*, 50:345–362, 2002.

[15] N. Paragios. Shape-based segmentation and tracking in cardiac image analysis. *IEEE Transactions on Medical Imaging*, 22(6):773–776, June 2003.

[16] J. Park, D. Metaxas, A. Young, and L Axel. Deformable models with parameter functions for cardiac motion analysis from tagged MRI data. *IEEE Trans. Medical Imaging*, 15:278–289, 1996.

[17] A. Pednekar, I.A. Kakadiaris, R. Muthupillai, and S.D. Flamm. Automatic hybrid segmentation of dual contrast cardiac MR images. In *Medical Image Computing and Computer-Assisted Intervention*, volume LNCS 2488, pages 690–697, Tokyo, Japan, September 25-28 2002.

[18] A. S. Pednekar and I.A. Kakadiaris. Adaptive fuzzy connectedness-based medical image segmentation. In *Proceedings of the Indian Conference on Computer Vision, Graphics, and Image Processing*, pages 457–462, Ahmedabad, India, December 16-18 2002.

[19] D. Rueckert and P. Burger. Geometrically deformable templates for shape-based segmentation and tracking in cardiac MR images. In *Energy Minimization Methods in Computer Vision and Pattern Recognition*, volume 1223, pages 83–98, Venice, Italy, 1997.

[20] A. Singh, D. Goldgof, and D. Terzopoulos. *Deformable Models in Medical Image Analysis*. IEEE Computer Society, Los Alamitos, CA, 1998.

[21] M. Sonka, B.P.F. Lelieveldt, S.C. Mitchell, J.G. Bosch, R.J. Van der Geest, and J.H.C. Reiber. Active appearance motion model segmentation. In *Second International Workshop on Digital and Computational Video*, pages 64–68, 2001.

[22] J.K. Udupa and S. Samarasekera. Fuzzy connectedness and object definition: theory, algorithms, and applications in image segmentation. *Graphical Models and Image Processing*, 58(3):246–261, 1996.

[23] N. Vlassis and A. Likas. A greedy EM algorithm for Gaussian mixture learning. *Neural Processing Letters*, 15(1):77–87, February 2002.